RESEARCH FOR THE BVI NOISE REDUCTION USING THE BLADE ACTIVE CONTROL

Masahiro Nakao , Naoki Uchiyama, Minoru Yoshimoto
Mitsubishi Heavy Industries, ltd. Nogoya, Japan
10 Oye-cho, Minato-ku, Nagoya 455-8515 Japan

Shigeru Saito, Natsuki Kondo
Japan Aerospace Exploration Agency (JAXA)
7-44-1, Jindaijihigashi-machi, Chofu, Tokyo 182-8522 Japan

Abstract

This paper presents the blade vortex interaction (BVI) noise reduction study using the blade active control. The study consists of the following three steps. As the first step, the BVI noise for the conventional blade was measured using Multi-Purpose Rotary Wing Test-rig (MPRT) in JAXA (Japan Aerospace Exploration Agency)[1]. It is important for the understanding BVI phenomena to know where the interaction between blade and vortex occurs. Sound pressure and blade surface pressure histories were obtained and the locations of the interaction were acquired. As the second step, prediction of BVI phenomena was tried using a noise prediction code. The simulation was done at the same condition of the BVI wind tunnel test and the comparison between numerical results and test data was done[2]. The quantative agreement between the test result and numerical one is still insufficient but interaction between the blade and vortex was able to be visualized. As the third step, active control rotor was developed and was evaluated the ability to reduce the BVI noise by the low speed wind tunnel test. Trailing edge flap is used to control the circulation of rotor blades to avoid strong interaction of blade and tip vortex. Active flap is controlled using piezoelectric actuators. The active rotor wind tunnel test was conducted in the same speed wind tunnel as the conventional rotor test. The effect of the active flap was rather small but further optimization of flap angle and location will improve noise reduction effect.

Nomenclature

C	= Speed of sound
C_T	= Rotor thrust coefficient
e	= Energy
J	= Jacobian
M	= Mach number
n	= Number of rotation of Main rotor
$\tilde{P}$	= Pressure
t	= Time
u,v,w	= x,y,z- velocity
V	= Flight velocity
x,y,z	= Spatial coordinates
α_s	= Rotor shaft angle (positive nose up)
θ	= Blade collective angle
μ	= Advance ratio, V/ ΩR
ξ, η, ζ	= Computational coordinate
ρ	= Density
τ	= Nondimensional time
ψ	= Blade azimuth angle

Introduction

Helicopter is one of the most convenient transportation. They can take us almost everywhere if enough space exist for landing or sling off us. The noise problem, however, barred wide spread use of helicopters. Most of the commercial use helicopters flies near the town. The aeronautics research is reducing noise to make helicopters more acceptable to the public. Active blade control method has been applied to reduce blade noise since 1970's. The effectiveness has been confirmed but the practical applications of such methods are not realized yet. The difficulty exists on the blade control method. Several methods have been developed for this thirty years. HHC(Higher Harmonic Control) and IBC (Individual Blade Control) are the famous blade control systems. HHC is the method to control a swash plate at high frequency to reduce vibration or rotor noise. IBC is the method to control each blade pitch angle individually. Active flap method can be called one sort of the IBC methods, however, conventional IBC methods use actuators between blade root and swash plate. High response and power are required for the IBC actuators. The merit of the active flap is that little force is required to control blade in comparison with conventional IBC method. The problem of the active flap method is developing the actuator, which is enough small to

be embedded in a narrow space of rotor blade, and has enough power to deflect flap to required angle at required frequency. Piezoelectric actuator and SMA(Shape Memory Alloy) have been developed for the active flap actuator. The former one has a high frequency actuation but has small displacement. The latter has a frequency actuation large power and displacement but has a low frequency actuation. In this study, piezoelectric actuator was selected as an active flap actuator and flap angle amplification mechanism was newly developed.

This paper presents the study of BVI noise reduction using active flap control. The study consists of three steps. The BVI noise for the conventional blade was measured in a wind tunnel as the first step. Prediction of BVI phenomena was tried using a noise prediction code, which consists of rotor CFD program and sound propagation analysis module as the second step. As the third step, active flap model rotor was developed and model rotor wind tunnel test was conducted in a low speed wind tunnel facility to obtain data in order to estimate the noise reduction effect of active flap method.

This study has been conducted under the joint research work between JAXA and Mitsubishi Heavy Industries, Ltd.

Basic Test

Basic data acquisition wind tunnel test was conducted in JAXA low speed wind tunnel.

Figure 1 Multi-Purpose Rotary Wing Test-rig (MPRT) in JAXA

The conventional rotor model was tested to acquire base noise data and BVI noise condition using Multi-Purpose Rotary wing Test-rig (MPRT) in JAXA (Japan Aerospace Exploration Agency) as shown in Fig.1.

The low speed wind tunnel facility in JAXA has 6.5m by 5.5m test section. The conventional model rotor has 2m diameter and four rectangular blades. Each blade has NACA0012 profiles and 8-degree twist. The wind tunnel test was performed with free stream velocity and the rotor angle of attack being the primary parameters. The blade pitch was cyclically controlled to achieve desired thrust amount. As output from the test, rotor six-component force, near leading edge pressure data and sound pressure history at fixed observation were measured. Figure 2 shows the schematic view of wind tunnel setting.

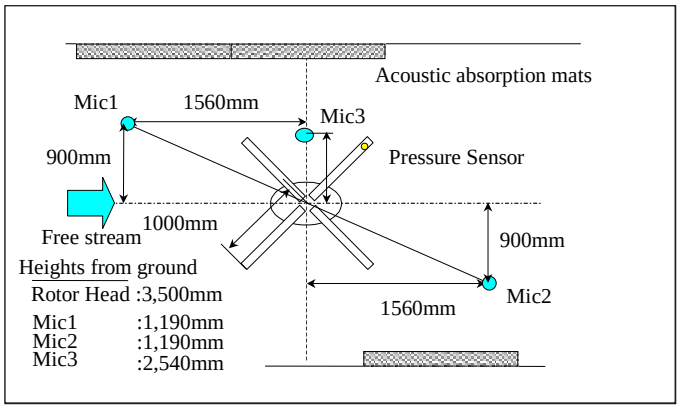

Figure 2 Schematic view of wind tunnel setting

Three microphones were used to measure the sound pressure histories as shown in Fig.2. Mic1 located about 1.5m ahead of the centre of the rotor. Mic2 located about 1.5m behind. Mic 3 located 0.8m beside. The height of each Mic is shown in Fig.3. Acoustic absorption mats were stuck on the wind tunnel wall in order to reduce the reflection of the noise. Test conditions are shown in Table 1.

Table 1 Test conditions

Rotor rotation speed:	1000 rpm
Flow velocity:	5 – 18.8 m/s (advance ratio 0.05 –0.18)
Rotor shaft angle	4 – 8 degree
Thrust coefficient Ct	0.008

Measured specific sound pressure profiles as a function of advance ratio and rotor shaft angle(a_s) are shown in Fig.3.Figure 3(a) shows the SPL obtained by Mic 1. The peaks of the SPL curves shift to the right according to the rotor shaft angle decrease. The same trend is shown in the plots of the other microphones.

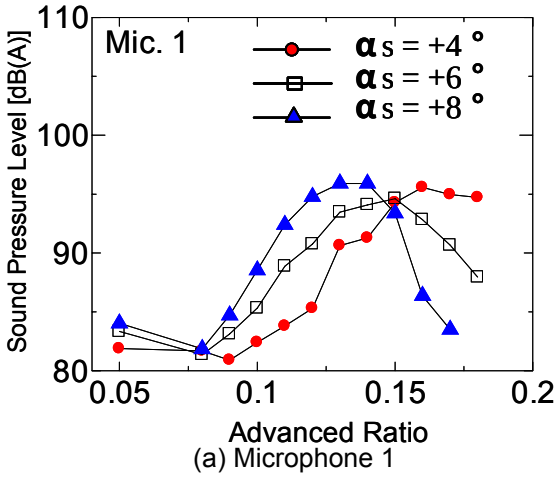

(a) Microphone 1

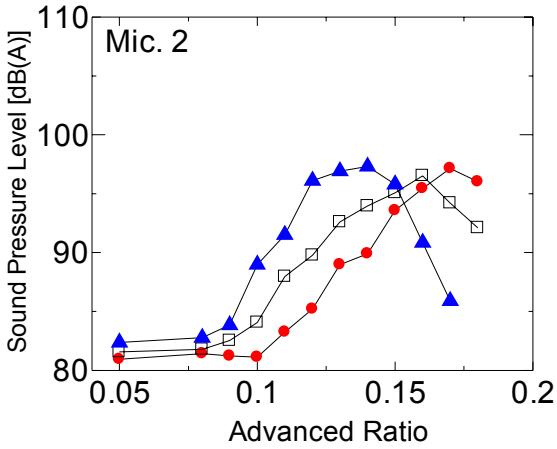

(b) Microphone 2

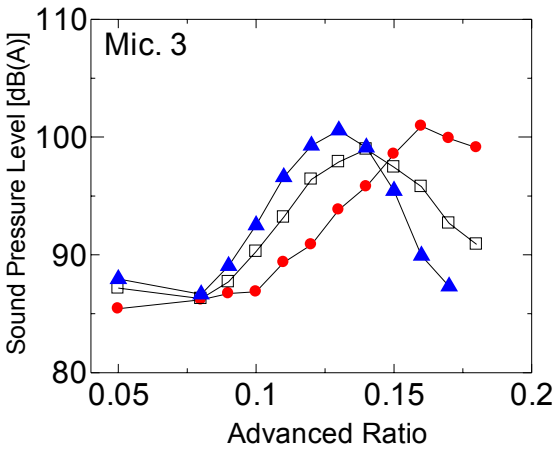

(c) Microphone 3

Figure 3 Specific sound pressure level

Typical acoustic waveforms obtained by Mic 3 at peak SPL conditions are shown in Fig.4.

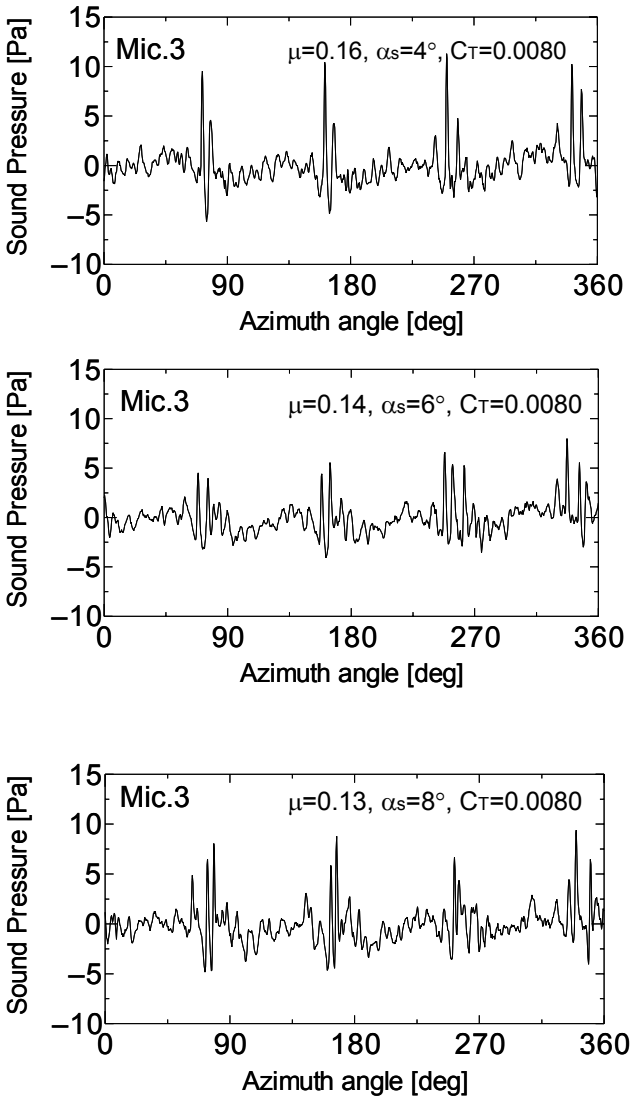

Figure 4 Typical acoustic waveforms

Figure 4 shows typical waveform at the peak SPL conditions as shown in Fig.3(c). The figure shows the strong BVI with the spiky peak of the acoustic waveform. These figures show the existence of BVI at peak region of SPL profiles. Especially, at the condition of advance ratio of 0.16 significant spiky wave appears at each blade rotation. Figure 5 shows the surface pressure histories as a function of blade azimuth angle.

The large change of the surface pressure was measured at the advancing side where the blade azimuth angle was about 53-degree as shown in Fig.5.

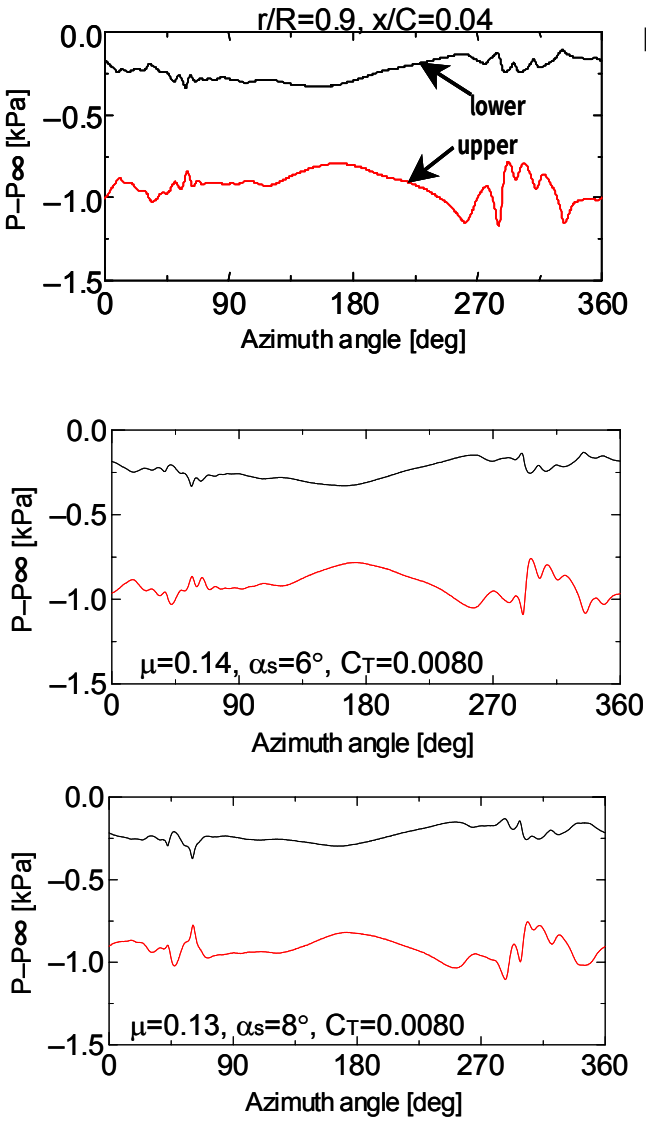

Figure 5 Blade surface pressure histories

In order to grasp the relation between BVI and the peak of sound pressure level, surface pressure peaks and geometrical BVI location are compared. Figure 6(a) shows a surface pressure history of blade lower surface. The numbers in circles express the peaks pressure, which correspond the numbers in Fig.6 (b). The relation between surface pressure and sound pressure is obtained by accounting the delay time from the sound source to the observation location. A top view sketch of the four-bladed rotor and tip vortices at the condition of circle number 2 is shown in Fig.6 (c).

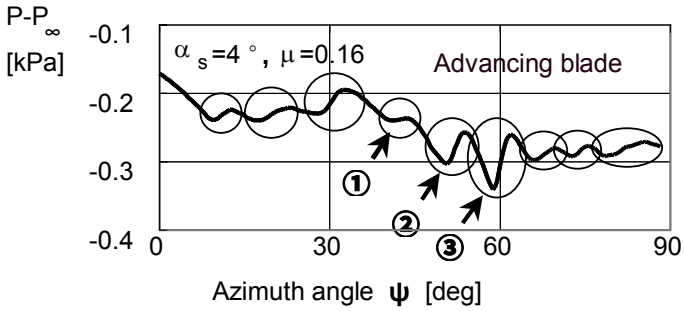

(a) Surface pressure history

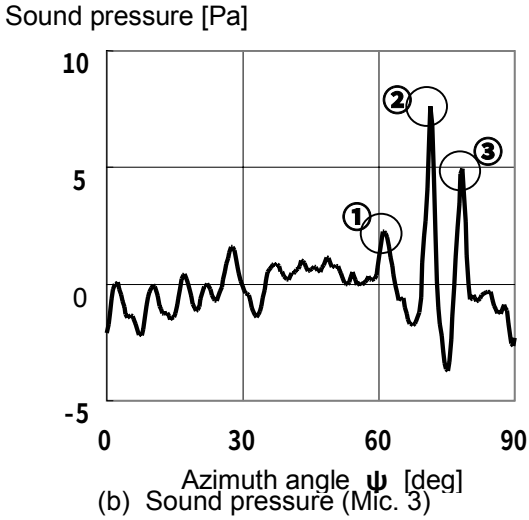

(b) Sound pressure (Mic. 3)

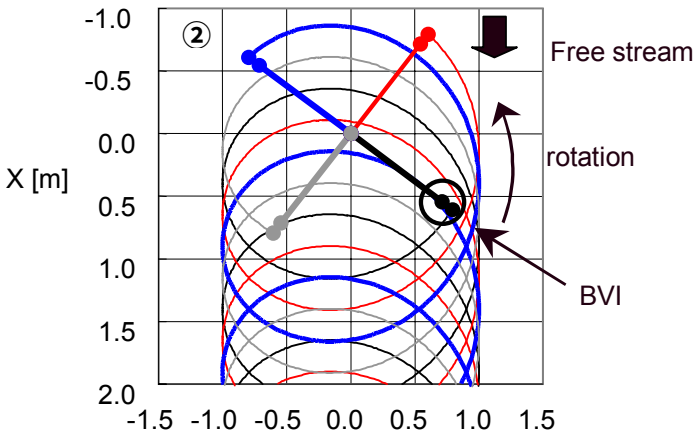

(c) Schematic view of rotor and tip vortex history

Figure 6 Relation between BVI, surface pressure and sound pressure

Figure 6(c) shows the parallel BVI at azimuth angle of about 60 degree. The differential pressure at the blade lower surface becomes negative because tip vortex interaction induces up wash at the leading edge. The large sound pressure change shown in Fig.6 (b).
These data show the relation between surface pressure change and sound pressure change.

BVI noise prediction

As the second step, BVI noise prediction was done for the model rotor in order to investigate the relation between the BVI and the measured sound pressure history. For most of the BVI prediction wake prediction method such as free wake code is used to calculate wake histories. In the present investigation CFD(Computational Fluid Dynamics) was used for 4 bladed rotor in BVI condition in order to validate its predictable ability. In estimating sound pressure history at fixed observation points, FW-H (Ffowcs-Williams and Hawkings) equation was solved with unsteady blade surface pressure distribution obtained form CFD results given as input. The details of CFD method are shown in the following section[3].

Governing Equations
The unsteady Euler equations take the form below.

$$\partial_\tau Q + \partial_\xi E + \partial \eta F + \partial_\zeta G = 0$$

$$Q = \frac{1}{J}\begin{bmatrix} \rho \\ \rho u \\ \rho v \\ \rho w \\ e \end{bmatrix}, \qquad E = \frac{1}{J}\begin{bmatrix} \rho U \\ \rho u U + \xi_x p \\ \rho v U + \xi_y p \\ \rho w U + \xi_z p \\ (e+p)U - \xi_t p \end{bmatrix},$$

$$F = \frac{1}{J}\begin{bmatrix} \rho V \\ \rho u V + \eta_x p \\ \rho v V + \eta_y p \\ \rho w V + \eta_z p \\ (e+p)V - \eta_t p \end{bmatrix}, \qquad G = \frac{1}{J}\begin{bmatrix} \rho W \\ \rho u W + \zeta_x p \\ \rho v W + \zeta_y p \\ \rho w W + \zeta_z p \\ (e+p)W - \zeta_t p \end{bmatrix},$$

Where,

$$U = \xi_t + u\xi_x + v\xi_y + w\xi_z,$$
$$V = \eta_t + u\eta_x + v\eta_y + w\eta_z,$$
$$W = \zeta_t + u\zeta_x + v\zeta_y + w\zeta_z,$$

$$\xi_t = -x_\tau \xi_x - y_\tau \xi_y - z_\tau \xi_z,$$
$$\eta_t = -x_\tau \eta_x - y_\tau \eta_y - z_\tau \eta_z,$$
$$\zeta_t = -x_\tau \zeta_x - y_\tau \zeta_y - z_\tau \zeta_z$$

The metric derivatives in time are required for grids attached to the blades that move against steady coordinate system. In the present approach, the motion of the blade is prescribed with harmonic functions which allows the analytical evaluation of the metric derivatives.

Grid System
The present approach makes use of over- lapped grid method. Each blade of the test model has its own computational grid to solve the flowfield within. The overall flowfield is obtained by successively interpolating the flow variable between the over-lapped grids. Figure 7 shows the computational grids around the wind tunnel model configuration. For this case, 4 grids are used to cover the model rotor, which consists of 4 blades.

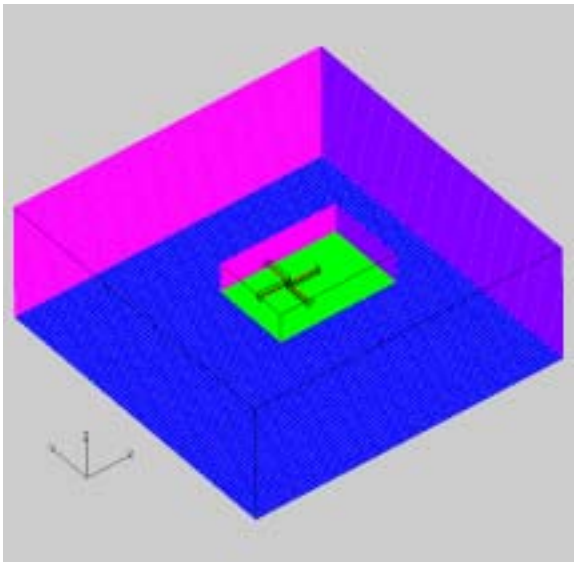

Figure 7. Computational grids around model configuration.

On the other hand, background Cartesian grid system that consists of two level exists to accurately capture the rotor wake. A dense grid with grid sizing of 0.1 of blade chord length C

covers the helicopter vicinity, while the coarse grid with its grid sizing 0.5C covers the whole computational domain. Total grid points for the present case amount roughly 30 million. Since the background grid holds the majority of the total grid points, in order to minimize the necessary computer storage, the use of coordinate array such as X(I,J,K), Y(I,J,K), Z(I,J,K) was successfully omitted by taking advantage of the uniform grid spacing.

Blade Motion

The cyclic motion of the blade can be considered as combination of feathering, flapping and lead-lag motions as pictured in Fig.8. In forward flight, feathering angle θ of the blade is cyclically controlled to maintain near constant lift throughout blade rotation, while the flapping angle β also varies cyclically to balance the moments generated by inertial, aerodynamic and centrifugal forces. Likewise, lead-lag angle ζ undergoes periodic changes in order to balance moments of inertial, aerodynamic, centrifugal and Coriolis forces.

In the present approach, these three motions were prescribed as first harmonic function with azimuth angle ψ. The coefficients in the harmonic functions were evaluated to give the best match against corresponding flight test data.

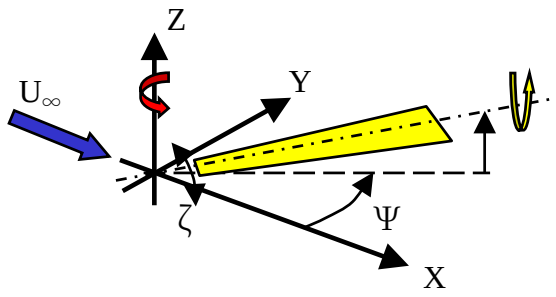

Figure 8. Description of the blade motion.

Numerical Scheme

The aerodynamic of the rotor is strongly influenced by its own wake. The tip vortex and the wake system may remain close to the rotor under particular flight condition, arising severe aerodynamic issues such as blade/vortex interaction. Therefore, for the CFD approach, it is essential to capture the unsteady rotor wake with high accuracy. Another aspect, which should be considered is the transonic effect. At high speed forward flight, unsteady shock wave can be formed near the tip of advancing side blade.

The computing of wake advection with high accuracy and capturing shock wave in a stable manner requires careful choice of the numerical scheme. In our approach, the upwind SHUS scheme[5] with the Osher-Chakravarthy extrapolation has been used in the blade, fuselage and tail component grids. The scheme posses stable shock capturing property with 3rd order accuracy in space. As for the background grids, 5th order space accurate scheme of Rai[6] has been used to specialize in capturing rotor wake. The 5th order accurate numerical flux takes the form below.

$$f_{i+\frac{1}{2}} = h_{i+\frac{1}{2}} + \frac{1}{120}\left(-6df^{+}_{i+\frac{3}{2}} + 48df^{+}_{i+\frac{1}{2}} + 22df^{+}_{i-\frac{1}{2}} - 4df^{+}_{i+\frac{3}{2}}\right)$$

$$-\frac{1}{120}\left(-6df^{-}_{i-\frac{1}{2}} + 48df^{-}_{i+\frac{1}{2}} + 22df^{-}_{i+\frac{3}{2}} - 4df^{-}_{i+\frac{5}{2}}\right)$$

Here, $df+$, $df-$ denote flux differences across positive and negative characteristic waves, respectively and h for the 1st order numerical flux.

Time Integration

The unsteady computation requires identical time steps for the entire computational grid points. Since the minimal grid spacing in the body fitted grid has smaller order than the uniform grid spacing of the background grid, the local CFL number varies rather wide among the two grid systems. In the present approach, LU-SGS implicit time stepping scheme was used for the grids around the helicopter components, while Runge-Kutta explicit time stepping scheme was used for the background grids. Since the grid attached to the moving blade solves for strong unsteady flow in nature, 2nd order time accurate formulation of below has been used in the LU-SGS scheme coupled with the Newton inner iteration method.

$$[\mathrm{LHS}]^{p}\left(Q^{p+1} - Q^{p}\right) = -\frac{2}{3}\Delta t\left[\frac{3Q^{p} - 4Q^{n} + Q^{n-1}}{2\Delta t} + (\mathrm{RHS})^{p}\right]$$

Interpolation Procedure

In the over-lapped grid approach, one has to successively interpolate the flow variables between the over lapping grids to obtain flowfield as a whole.

This process can become time consuming especially with the moving grids. The identification of inclusive relation on each grid point to the other grid system generally requires a seeking process. However, the process can be simplified if either of the grid system is Cartesian with uniform grid spacing. We have circumvented the direct interpolation process between the two body fitted grids, for instance between blade grid and the fuselage grid. Instead, the background dense Cartesian grid was used to translate such process in between. With this approach, every body fitted grid point can address its location explicitly in the underlying Cartesian grid. This minimizes the interpolation process greatly and contributes significantly to achieve efficient computation.

In the present analysis, space of background grid is set to 0.15C(C:chord length) and each time step is correspond to 0.1 degree of blade azimuth angle.

Sound analysis

In estimating sound pressure history at fixed observation points, FW-H (Ffowcs-Williams and Hawkings) equation known as Farassat's Formulation 1A was chosen as the theoretical basis was solved with unsteady blade surface pressure distribution obtained form CFD results given as input.

$$4\pi P_L(x,t) = \frac{1}{c}\int_{surf}\left[\frac{\dot{\mathbf{p}}\cdot\mathbf{r}}{r(1-M_r)^2}\right]_{ret} ds + \int_{surf}\left[\frac{\mathbf{p}\cdot(\mathbf{r}-\mathbf{M})}{r^2(1-M_r)^2}\right]_{ret} ds + \frac{1}{c}\int_{surf}\left[\frac{(\mathbf{p}\cdot\mathbf{r})(r\mathbf{r}\cdot\dot{\mathbf{M}}+cM_r-cM^2)}{r^2(1-M_r)^3}\right]_{ret} ds$$

Where **P** is the air load vector on the blade surface, **r** is the unit vector from the blade surface to the observation point and *r* denotes the distance. **M** is the local Mach number of the blade surface, which is nondimensionalized by speed of sound in the free stream. *Mr* denotes the inner product of **M** and **r**. Each term is integrated in terms of whole blade surface.

Results

The computation was chosen for the corresponding BVI wind tunnel test which has been performed for the conventional rotor. Likewise, CFD computation was performed and was validated against these corresponding data. Table 1 shows the blade cyclic angle coefficients. In order to set calculated rotor thrust coefficient Ct to 0.008 which is corresponded to the measured thrust at wind tunnel test, collective pitch angle is increased in comparison with that of wind tunnel data.

Table 1 Blade cyclic angle coefficients

	θ_0	A_1	B_1
WTT	12.3	-3.2	2.6
CFD	14.0	-3.2	2.6

$$\theta = \theta_0 - A_1(\psi) - B_1\sin(\psi)$$

Figure 9 shows rotor thrust history versus blade azimuth angle. The thrust coefficient is periodically changed near the Thrust coefficient Ct.

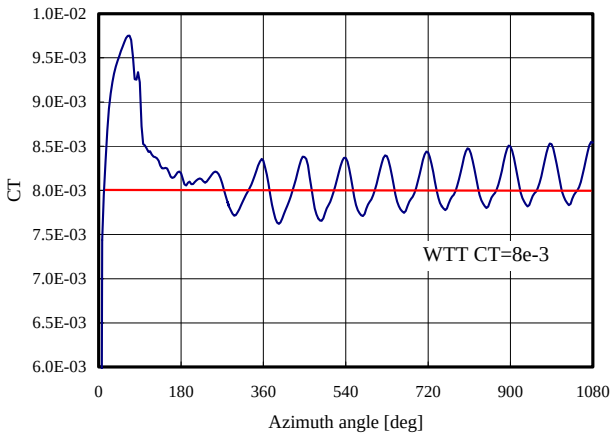

Figure 9 Rotor thrust history

Figure 10 shows the surface pressure history at the blade leading edge. Peaky pressure profile is not shown in the numerical results as shown in experimental data(Fig.5).

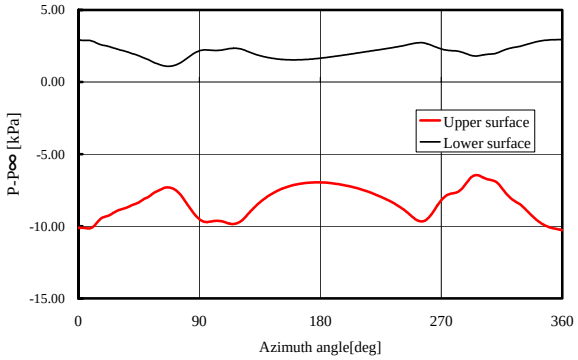

Figure 10 Surface pressure history

Figure 11 shows the calculated sound pressure history at the observation point of Microphone 3. The figure shows the profile of 1st term of FW-H equation which is considered for especially contribution of BVI, and the profile of the sum of the 2nd and the 3rd terms.

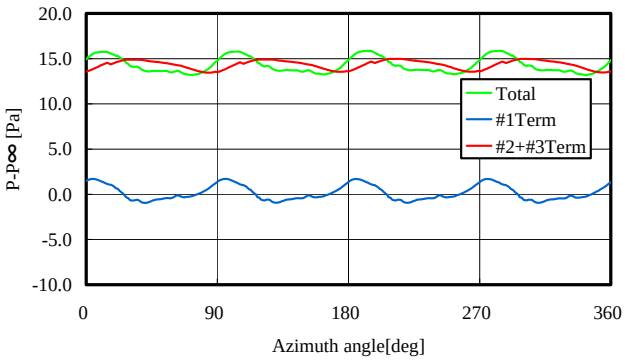

Figure 11 Sound pressure history

Figure 12 shows the comparison of sound pressure history between numerical result and experimental data. The experimental data and the sum of 2nd and 3rd terms of numerical results are plotted. The spiky pressure peaks of experimental data are not captured in numerical results. The aerodynamic phenomenon by BVI interference itself is considered not to yet be resolved fully.

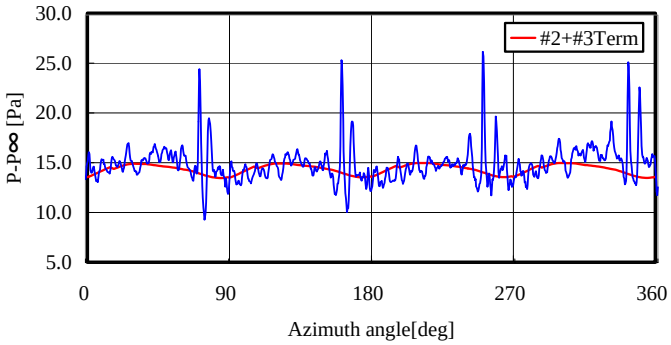

Figure 12 Comparison of sound pressure history

Figure 13 shows the calculated instantaneous iso-vorticity surface at the four-bladed rotor disc. Visually, the BVI phenomenon is captured by CFD. Figure 14 shows the vortices shed from the blade tip at the cross section shown as red line in Fig.13. The tip vortex faded out with the vortex age.

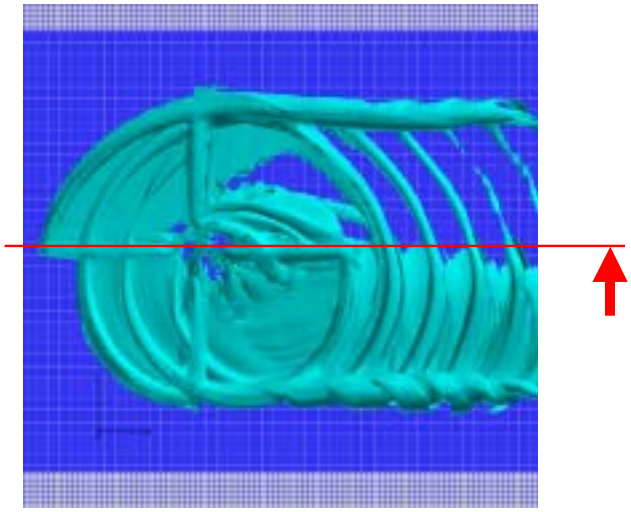

Figure 13 Iso-vorticity surface

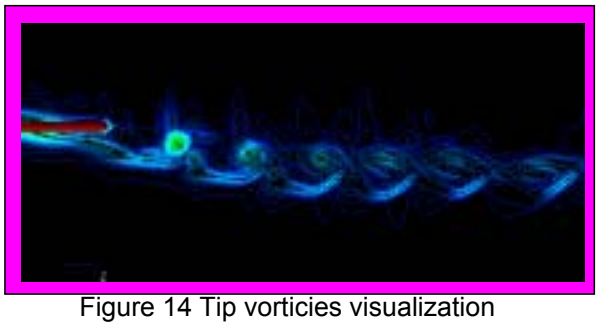

Figure 14 Tip vorticies visualization

Figure 14 shows 6th vortex age and the strength of vortex core become weaker and weaker with its age. Spiky sound pressure change is generated from the rapid change of the surface pressure by BVI. The strength of vortex core plays an important role. The resolution of tip vortex core calculated by CFD depends on the background grid fineness. In this study, a higher order scheme and a large size background grid are applied for higher resolution. The results, however, show that the simulation is still insufficient to calculate BVI sound wave form. Further refinement of the method is future work.

Active flap wind tunnel test

As the third step, an advanced rotor model with the active flaps at the blade trailing edges was developed as shown in Fig.15.

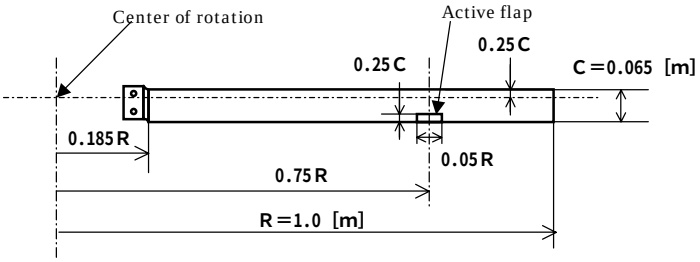

Figure 15 Schematic view of active flap blade

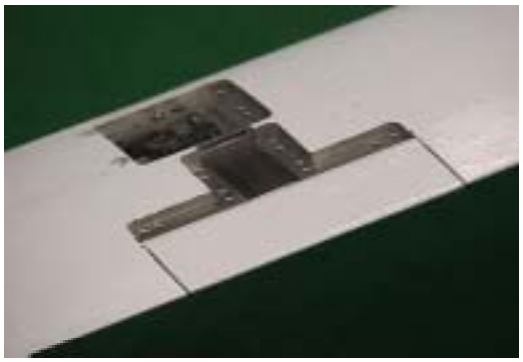

Figure 16 Close up view of active flap

The active flap is driven by a piezoelectric actuator embedded in the blade. The length of the flap is 5% blade span and the center of the trailing edge flap locates 75% blade span. The maximum flap deflection is about 2 degree and flapping frequency is up to 40Hz. The active control blade has rectangular planform, 8 degree twist and NACA0015 section airfoil. The rotor has two blades and one of them has two pressure taps near the leading edge of lower surface. The acoustic wind tunnel test was conducted in the same wind tunnel for the conventional rotor. The BVI noise was measured with and without active flap control. Test conditions are shown in Table 3.

Table 3 Test conditions

Rotor rotation speed:	800 rpm
Flow velocity:	0 – 20.9 m/s (advance ratio 0.0 –0.25)
Rotor shaft angle	1 – 10 degree
Thrust coefficient Ct	0.0032-0.004

The wind tunnel test was conducted in the same low speed wind tunnel in JAXA where the basic BVI test was conducted. Figure 17 shows the picture of the test facilities.

Figure 17 Picture of wind tunnel facility

In advance of the test, it searched for the advance ratio conditions that BVI noise becomes large based on prediction by geometric examination. Figure 18 shows the schematic view of advancing side rotor and BVI occurred at the blade azimuth angle of about 60 degree.

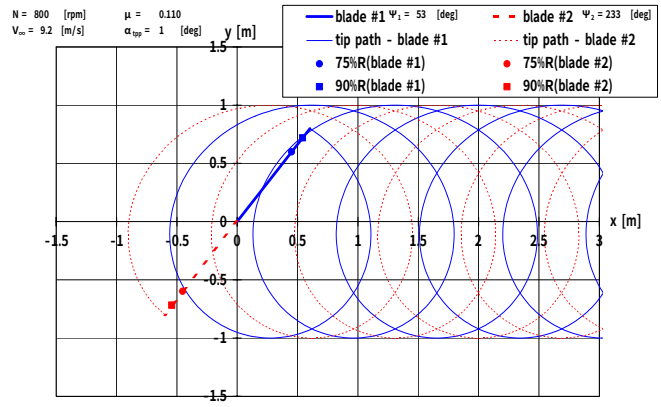

Figure 18 Schematic of blades and tip vorticies histories (advancing side)

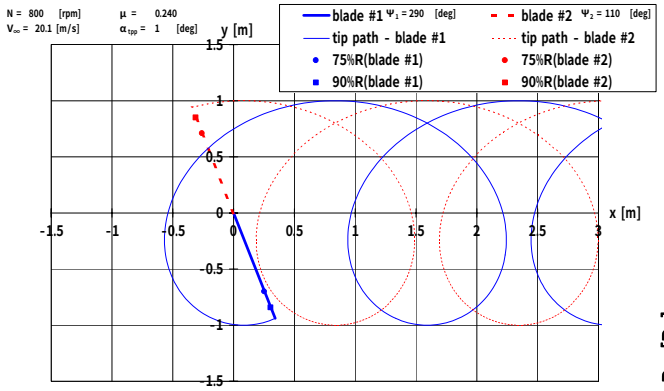

Figure 19 Schematic of blades and tip vorticies histories(retreating side)

Figure 19 shows the schematic view of retreating blade. The BVI occurred at the blade azimuth angle of about 250 degree.
The waveform at advancing side BVI condition is shown in Fig.20. The figure includes the waveform of no BVI condition of advance ratio of 0.21. Spiky peaks are shown the plot of advance ratio of 0.17.

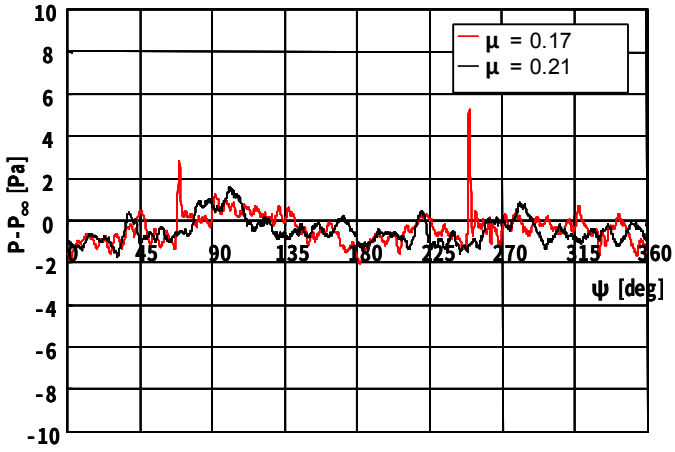

Figure 20 Comparison of waveform between BVI and no BVI conditions at advancing side.

The waveform at retreating side BVI condition is shown in Fig.21. Comparison with advancing side waveform, spike of the waveform is rather small.
The peaks appear at azimuth angles of 140 and 320 degree.

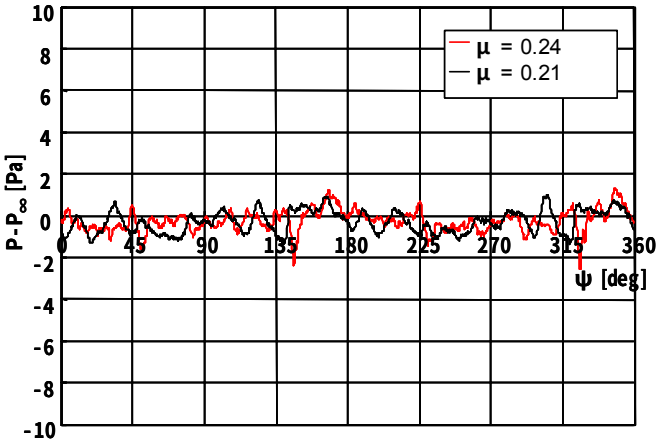

Figure 21 Comparison of waveform between BVI and no BVI conditions at retreating side.

Figure 22 shows the power spectrum of 1/3 octave band analysis with advance ratio of 0.14 to 0.21.

Comparison of power spectrum between BVI and no BVI conditions is shown in the figure. The figure shows that the frequency of the BVI appears at the bandwidth form 600 to 2000 Hz.

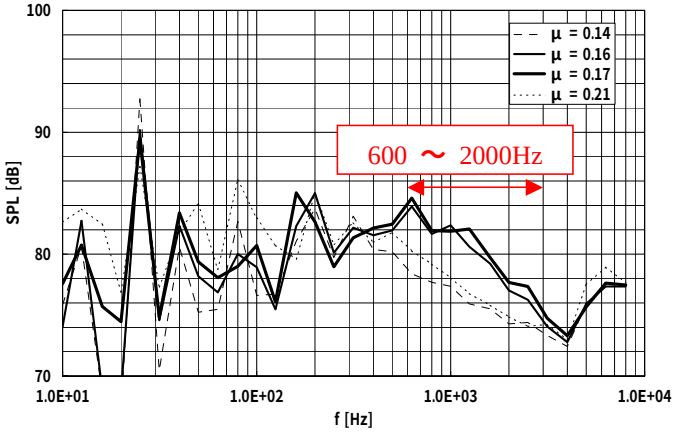

Figure 22 Power spectrum

Figure 23 shows the active flap control waveforms. The rectangular wave and sine wave were tested. The phase angle of the flap versus blade azimuth angle is one of the test parameter. The frequency of the flap is also the parameter.

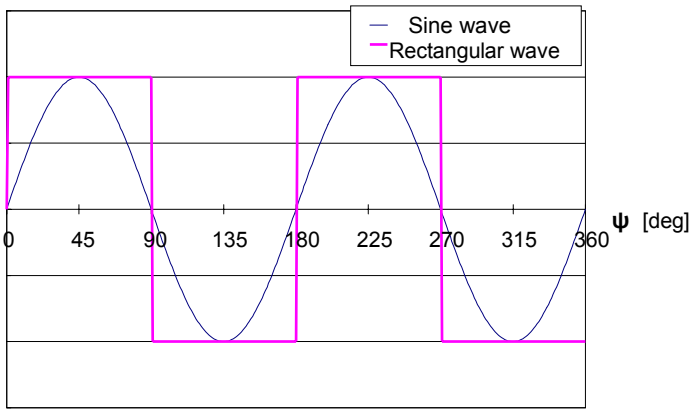

Figure 23 Active flap control waveform

The results are shown in Figs.24 and 25. The horizontal axis shows the phase angle of flap versus blade azimuth angle. The vertical axis shows the difference of BVI sound pressure level between flap control on and off. Figure 24 shows the advancing side and Figure 25 shows retreating side. The plots show rectangular wave deflection is effective in comparison with sine wave generally. The effect is appeared for advancing side as shown in Fig. 24 but effect is not shown in retreating side as shown in Fig.25. The maximum reduction of BVI noise is up to 0.6dB as shown in Fig.24(b). In this study, active flap location and size are not optimized. Further improvement for noise reduction would be the future work.

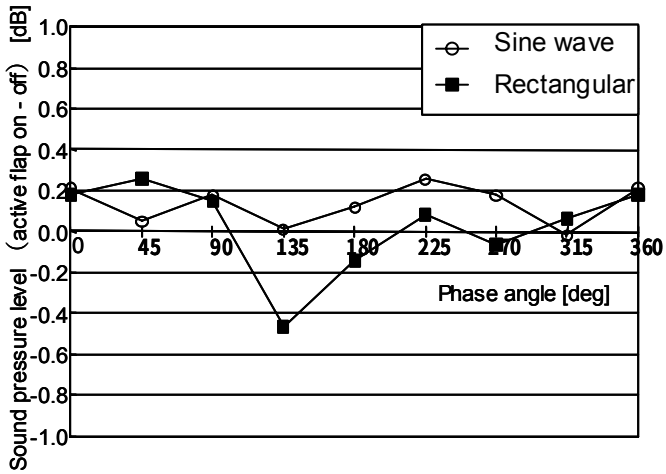

Figure 24(a) Effect of active flap(2/rev)

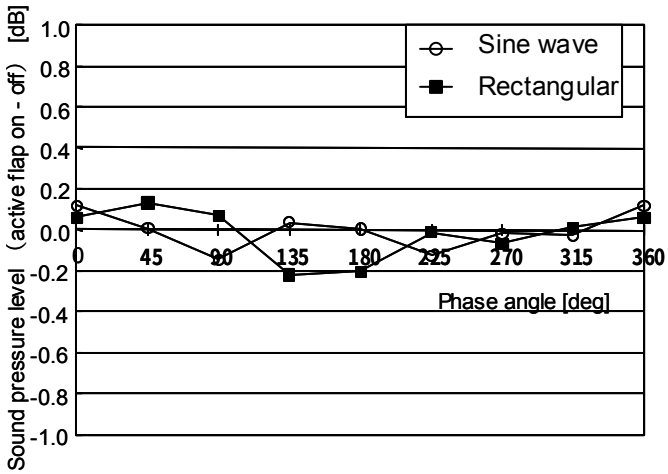

Figure 24(b) Effect of active flap(3/rev)

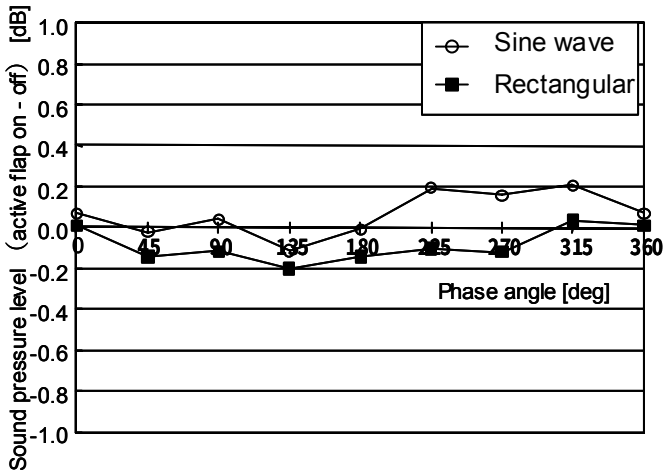

Figure 25(a) Effect of active flap(2/rev)

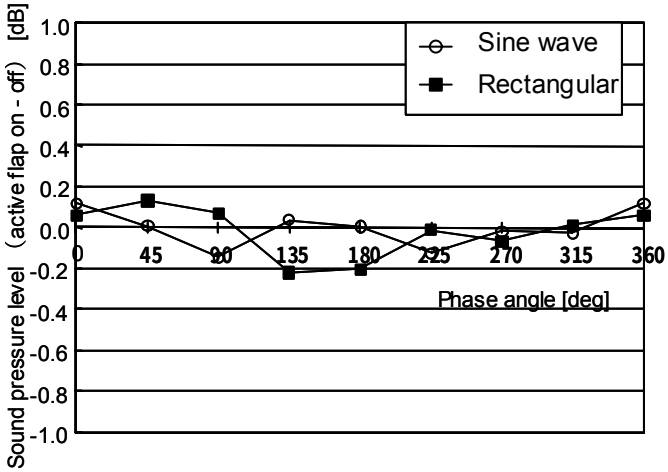

Figure 25(b) Effect of active flap(2/rev)

Concluding Remarks

The blade vortex interaction (BVI) noise reduction is studied using the blade active control. The study was proceeded at three steps. As the first step, the BVI noise for the conventional blade was measured. Sound pressure and blade surface pressure histories were obtained and the locations of the interaction were acquired. As the second step, prediction of BVI phenomena was tried using a noise prediction code. The simulation was done at the same condition of the BVI wind tunnel test and the comparison between numerical results and test data. As the third step, active control rotor was developed and was estimated the ability to reduce the BVI noise by the low speed wind tunnel test. The effect of the active flap was rather small but further optimization of flap angle and location will improve noise reduction effect.

References

(1) Nakao, M., Uchiyama, N., Ichiro Maeda, I., Hattori, K., Saito, S., Aoyama, T., Kondo, N., "Research for the BVI noise reduction using the Blade Active Control," Aircraft symposium 2003.

(2) Nakao, M., Uchiyama, N., Maeda, I., Saito, S., Aoyama, T., Kondo, N., "On Helicopter BVI Noise Prediction," NAL SP-57 2003.

(3) Uchiyama, N., "Development on Unsteady Aerodynamic Code for Helicopter Configuration, " Heli Japan 98.

(4) Uchiyama, N., and Fujii, K., "A Flowfield Analysis of a Simple Helicopter Shape, ' Proc. of 15th NAL Symposium on Aircraft Computation Aerodynamics," NAL SP-45, pp.95-100.

(5) Shima, E. and Jounouchi, T., "Role of Computational Fluid Dynamics in Aeronautical Engineering(No.12),"' on Aircraft Computation Aerodynamics, NAL SP-27, pp.255-260.

(6) Rai, M. M., "Navier-Stokes Simulations of Blade-Vortex Interaction Using High-Order Accurate Scheme," AIAA-87-0543, 1987.